Investigation on hydrodynamic characteristics of a hydrofoil based on γ-$Re_{\theta t}$ transition model

Investigation on hydrodynamic characteristics of a hydrofoil based on γ-$Re_{\theta t}$ transition model

Investigation on hydrodynamic characteristics of a hydrofoil based on γ-$Re_{\theta t}$ transition model

Changliang Ye[1,2], Fujun Wang[2], Yuan Zheng[1], Daqing Zhou[1], B P M van Esch[3]
[1] College of Energy and Electrical Engineering, Hohai University, Nanjing, 211100, PR China
[2] College of Water Resources and Civil Engineering, China Agricultural University, Beijing, 100083, PR China
[3] Department of Mechanical Engineering, Eindhoven University of Technology, Eindhoven, 5600MB, the Netherlands
E-mail address: yechangliang@hhu.edu.cn

Abstract. The complex flow field caused by the dynamic stall can affect the operational stability of hydrodynamic machinery. In this paper, the NACA0009 blunt trailing edge hydrofoil is used as the object of study, and the dynamic stall characteristics of the hydrofoil are investigated by using the transition model and the dynamic mesh method. It is found that the hydrofoil deep stall calculated by the transition model is delayed compared to that calculated without the transition model. The hydrofoil dynamic stall can be divided into four stages, initial stage, development stage, stall inception stage and deep stall stage. In the initial stage and the development stage, the lift and drag characteristics are influenced by the shedding vortex. In the stall inception stage and the deep stall stage, the lift and drag characteristics are influenced by the leading edge separation vortex and the trailing edge vortex. The increase of angular velocity and Reynolds number of the dynamic hydrofoil delay the onset of the deep stall while accelerating the boundary layer transition. The research in this paper has a certain guiding effect for the safe and stable operation of hydrodynamic machinery.

1. Introduction

In axial-flow turbines, runner blades and guide vanes rotate continuously with the change of load, and the stability of the flow structure dynamic characteristics during the adjustment of the blade angle from non-coincident to concurrent conditions is a key issue to ensure the normal operation of the hydraulic unit [1]. The dynamic changes of the guide vanes are often accompanied by a complex transient flow field, which in turn causes water strike fluctuations in the upstream piping system and affect the transient characteristics of the downstream runner blade path [2].

The propellers of ships, and the blades of axial impeller machinery are designed based on hydrofoils, and the discussion of hydrofoil hydrodynamic characteristics is of great significance for the design of blades and hydrofoils [3]. The boundary layer transition is the dominant flow state on the hydrofoil surface at small angles of attack, and when the angle of attack increases, the hydrofoil undergoes a laminar-induced transition which generates leading edge separation vortices. The transition is completed rapidly at the leading edge of the hydrofoil as the angle of attack continues to increase, so the transition is a major influence on hydrofoil performance and has a significant effect on the location of flow separation and the growth of separation vortices [4]. Zhang [5] found that using the transition model was able to predict the lift and drag characteristics of a Clark-Y hydrofoil more accurately at a Reynolds number of 4.4×10^5. Almohammadi [6] found that the generation of laminar separation bubbles could only be predicted when a transition model was introduced for a dynamic stall study of a vertical axis

wind turbine. If the transition effect is not considered in the design or optimization process, the error in energy conversion caused by laminar separation bubbles is as high as 20%. Seyednia [7] found that the inaccuracy of the pressure distribution of the S809 aerofoil at an angle of attack of 5.13º was also solved when the transition was taken into account in the calculation. In the hydraulic machinery investigations, Rijpkema [8] studied the scaling effect of marine propellers and found that the predicted efficiency errors ranged from 15% to 35% at different Reynolds numbers, and the analysis suggested that the performance differences could be related to the incorrect capture of transition on the blades. In the studying water-jet pumps, Li [9] found that considering the effect of transition in numerical simulations improved the predictions of the pressure distribution and friction coefficient distribution at the blade surface compared to turbulence models that did not consider the transition effect. Bhattacharyya [10-11] considered the transition effect and used a sliding mesh approach in predicting the performance of a marine ducted propeller, and the predicted streamlines successfully showed the transition region.
Hydrofoil boundary layer transition may induce flow separation or vortex [3], so it is important to accurately predict the location of boundary layer transition, which is helpful for the design of hydrodynamic machinery. In this paper, the NACA0009 blunt trailing edge hydrofoil is used to study the dynamic stall characteristics, also, the transition model and dynamic mesh method are applied.

2. Turbulence Modelling

In the SST k-ω turbulence model, the transport equations for the turbulent kinetic energy k and the turbulent specific dissipation rate ω are conserved in the form

$$\frac{\partial}{\partial t}(\rho k)+\frac{\partial}{\partial x_i}(\rho k\overline{u}_i)=\frac{\partial}{\partial x_j}\left(\Gamma_k\frac{\partial k}{\partial x_j}\right)+G_k-Y_k+S_k \tag{1}$$

$$\frac{\partial}{\partial t}(\rho \omega)+\frac{\partial}{\partial x_i}(\rho \omega\overline{u}_i)=\frac{\partial}{\partial x_j}\left(\Gamma_k\frac{\partial \omega}{\partial x_j}\right)+G_\omega-Y_\omega+D_\omega+S_\omega \tag{2}$$

The SST γ-$Re_{\theta t}$ transition model proposed by Langtry and Menter [12] is constructed using local variables. The model is based on the two-equation SST k-ω turbulence model and two additional transport equations. One is the intermittency factor γ equation, which is used to control the transition length. The other is the transport equation for the momentum thickness Reynolds number $\tilde{Re}_{\theta t}$, used to trigger the transition. They are as follows:

$$\frac{\partial\left(\rho\tilde{Re}_{\theta t}\right)}{\partial t}+\frac{\partial\left(\rho U_j\tilde{Re}_{\theta t}\right)}{\partial x_j}=P_{\theta t}+\frac{\partial}{\partial x_j}\left[\sigma_{\theta t}\left(\mu+\mu_t\right)\frac{\partial\tilde{Re}_{\theta t}}{\partial x_j}\right] \tag{3}$$

$$\frac{\partial(\rho\gamma)}{\partial t}+\frac{\partial\left(\rho U_j\gamma\right)}{\partial x_j}=P_\gamma-E_\gamma+\frac{\partial}{\partial x_j}\left[\left(\mu+\frac{\mu_t}{\sigma_f}\right)\frac{\partial\gamma}{\partial x_j}\right] \tag{4}$$

When the transition model is coupled with the SST k-ω model, the production and destruction term of the k equation are changed. In addition, an intermittency γ_{sep} is introduced for predicting separation induced transition. The combinations are shown below:

$$\frac{\partial\rho k}{\partial t}+\frac{\partial\left(\rho U_j k\right)}{\partial x_j}=\tilde{P}_k-\tilde{D}_k+\frac{\partial}{\partial x_j}\left(\left(\mu+\sigma_k\mu_t\right)\frac{\partial k}{\partial x_j}\right) \tag{5}$$

$$\tilde{P}_k=\gamma_{eff}P_k,\quad \tilde{D}_k=\min\left(\max\left(\gamma_{eff},0.1\right),1.0\right)D_k \tag{6}$$

where, P_k and D_k are the original production and destruction terms from the SST k-ω turbulent kinetic energy equation.

3. Numerical simulation

3.1 Solution strategy

The research object of this paper is the NACA0009 blunt trailing edge hydrofoil. As shown in Figure 1, the computational domain is divided into two regions with the fixed grid and the moving grid. In order to realize the dynamic change of the angle of attack, the grid moving region is centered on the center of gravity of its hydrofoil and rotates around the center of the hydrofoil according to the given angular velocity. The interface is set between the grid moving region and the grid fixed region. A slip-free interface is used at the boundary of the circular region of the hydrofoil, so that a relative angular displacement can be achieved between the grid fixed region and the grid moving region.

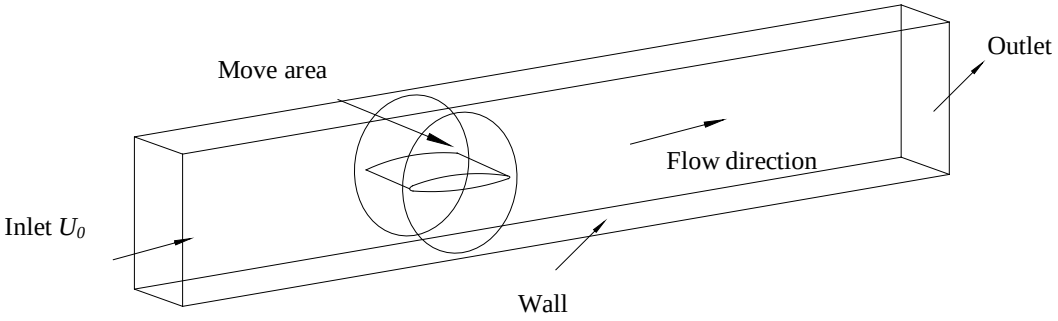

Figure 1 Hydrofoil dynamic stall speed calculation domain settings

The computational domains are all meshed with a hexahedral grid, where the number of non-moving region grids is 3.7×10^7 and the number of moving region grids is 2.5×10^7, and 500 nodes are set in the hydrofoil boundary layer to satisfy $y+\approx 1$. The time step of the simulation is chosen to be 1×10^{-5}s, which ensures that the average Courant number (CFL) ≈ 1. The angular velocity of the moving region of the grid is defined by ANSYS CFX expression language. This part of the computational work was run at the High-Performance Computing Centre of the Eindhoven University of Technology (TU/e) using 256 GB of memory and 128 cores for parallel computation.

3.2 Validation

The characteristics of the NACA0009 dynamic hydrofoil were studied in a cavitation water tunnel at the Swiss Federal Institute of Technology in Lausanne [13]. An oscillation system is used to generate different values of oscillation frequency and amplitude. The drive system can generate oscillations with frequencies up to 50 Hz. The angle of attack variation is adjusted between 0° and 10°. Pressure sensors are installed on the hydrofoil surface and 12 monitoring points are arranged, as shown in Figure 2.

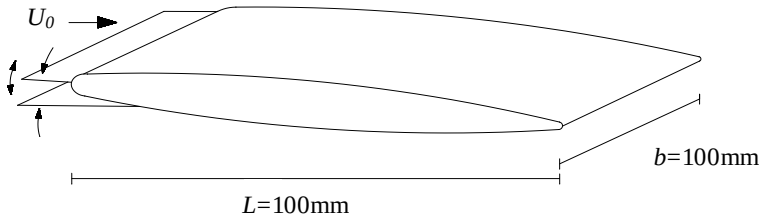

(a) Experimental hydrofoil

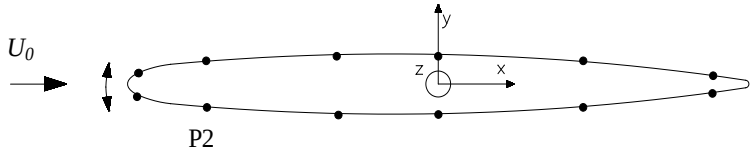

(b) Arrangement of experimental pressure measurement points

Figure 2 Dynamic hydrofoil experimental device [13]

The experimental results of the pressure monitoring point P2 in one cycle for the pressure coefficient *Cp* are compared with the numerical simulation results in Figure 3. It can be seen from Figure 3 that the simulated and experimental values match well in terms of the trend of the pressure coefficient and the specific values in one cycle time, which verifies the reliability of the method used for the numerical calculation.

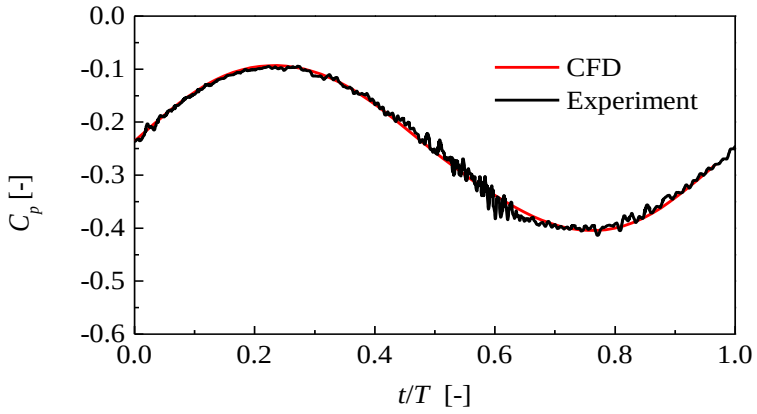

Figure 3 Comparison of experimental and numerical pressure coefficients at P2

4. Results

4.1 Dynamic hydrofoil lift &drag and stall characteristics

Figure 4 shows the comparison of lift and drag coefficients between the turbulence model with transition and the turbulence model without transition for the Reynolds number Re_L=2.0×10^6. It can be seen that the difference between the two models is small before the stall inception, and the magnitude of the drag coefficient and the oscillation range after the stall are much different, and the hydrofoil deep stall predicted by the turbulence model without transition is significantly earlier. In the study of NACA66 (mod)-312 hydrofoil [14], it was found that the transition model has certain advantages in the prediction of laminar separation bubbles, and the turbulence model without transition has large errors in the laminar separation-induced transition near the leading edge of the suction side.

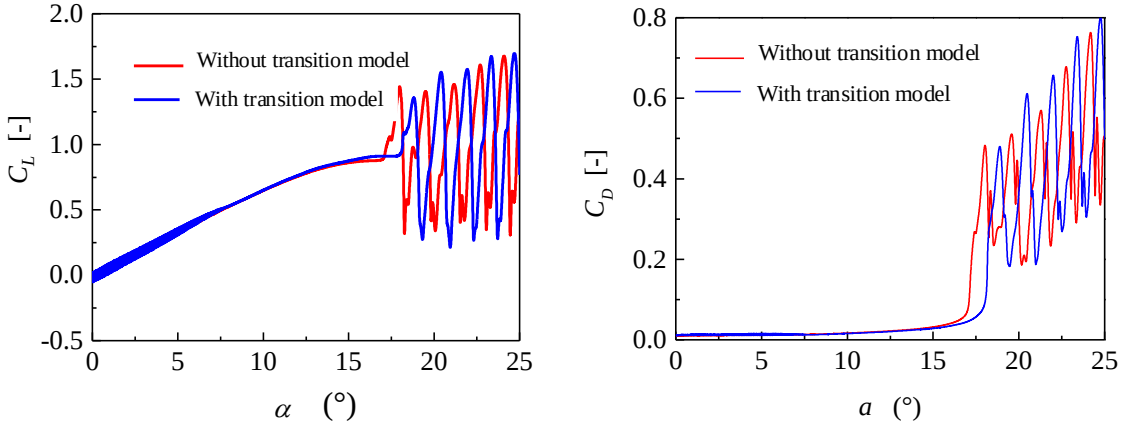

(a) Lift coefficient C_L (b) Drag coefficient C_D

Figure 4 Variation of lift and drag coefficients with angle of attack using different models

Dynamic stall characteristics of the hydrofoil with the change of angle of attack can be divided into the following four characteristic stages: initial stage (α = 0° ~ 7.8°): During this stage, the lift coefficient and drag coefficient have a linear growth trend as the angle of attack increasing, and there is a small oscillation of the lift and drag coefficient in a certain range. From Figure5 (a), the shedding vortices is existence in the wake region, which results in the oscillation of the lift and drag coefficient. Development stage (α=7.8°~14.6°): During this stage, the lift and drag coefficient still grows linearly but the trend

becomes slower, and the oscillation disappears. As can be seen from Figure 5(b), at this time, the shedding vortex near the trailing region disappears, which may result in the oscillation disappearance of the lift and drag coefficient.

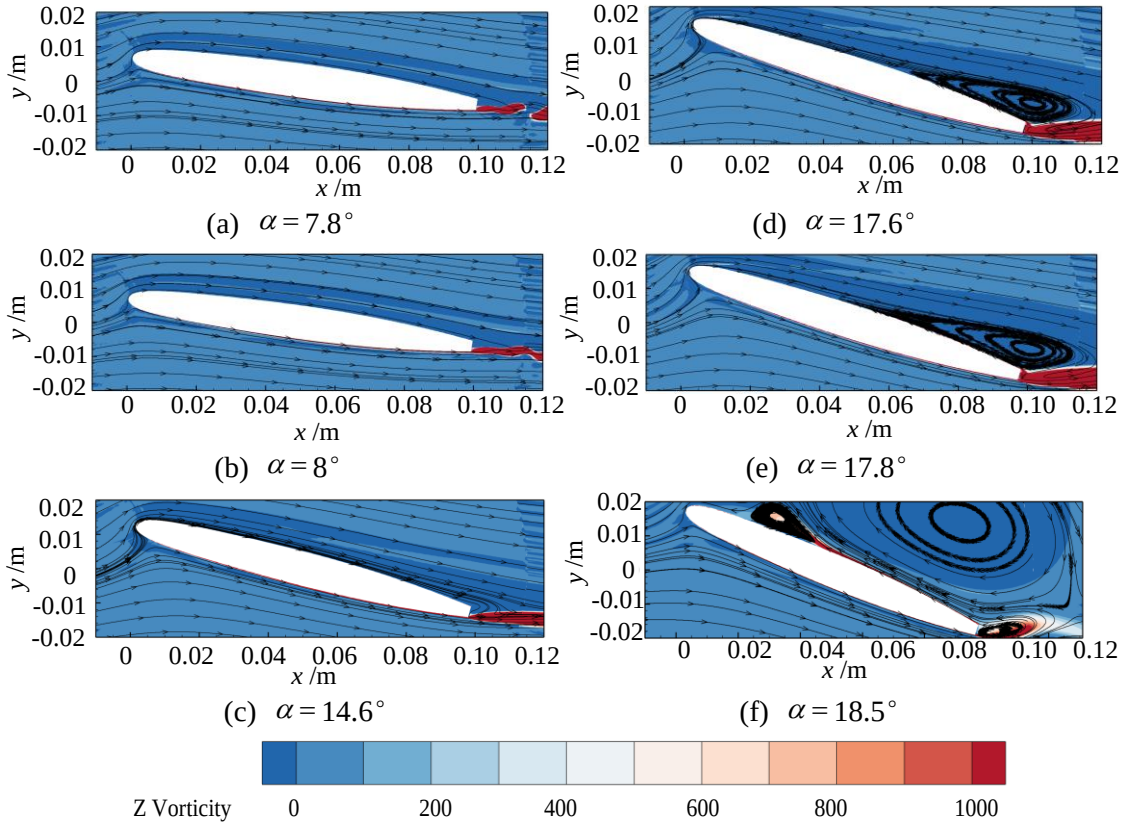

Figure 5 Dynamic hydrofoil flow field streamline distribution and vortex distribution

Stall inception stage (α=14.6°~17.6°): During this stage, the lift and drag coefficient of the hydrofoil changes gently. It can be seen from Figure 5 (c), that the flow separation is found at the trailing edge of the hydrofoil suction side. The hydrofoil pressure side is affected by the positive pressure gradient, which offset the impact caused by the hydrofoil trailing edge separation vortex, and thus the curve changes gently at this stage. Deep stall stage (α=17.6° ~ 25°): As can be seen from Figure 4, the lift and drag characteristics show an obvious oscillation trend due to the formation of the leading edge vortex and the trailing edge vortex on the suction side. When the trailing edge vortex and the leading edge vortex development to the maximum extent, fully attached to the entire suction side, at which time the lift and drag coefficient reaches its maximum. When the leading edge vortex has the opposite direction of the trailing edge vortex, the lift and drag coefficient reach the minimum value. When the leading edge vortex and trailing edge vortex are moving to the downstream, a new trailing edge vortex and leading edge vortex will appear, and a new cycle process will begin. In summary, the development and evolution of the leading edge vortex and trailing edge vortex lead to fluctuations in the lift and drag characteristics of the hydrofoil.

4.2 Effect of angular velocity on dynamic stall characteristics

To investigate the effect of angular velocity variation on the dynamic hydrofoil stall, this section calculates and analyses the dynamic hydrofoil at three angular velocities (40°/s, 80°/s and 160°/s) with an inlet velocity of 20 m/s, corresponding to a Re_L of 2.0×10^6. Figure 6 shows the variation curves of the lift and drag coefficient with the angle of attack for the three angular velocities. The convergence check process is consistent with the previous text. It can be seen that lift and drag characteristics still present four stages as the angular velocity changing. In the first two stages, the drag coefficient is not affected by the angular velocity, while the lift coefficient increases with the increase of angular velocity.

In the fourth stage, the angles of attack of the deep stall corresponding to 40°/s, 80°/s and 160°/s are 17.5°, 18.1° and 18.8°, respectively, which indicates that the increase of angular velocity delays the generation of hydrofoil stall.

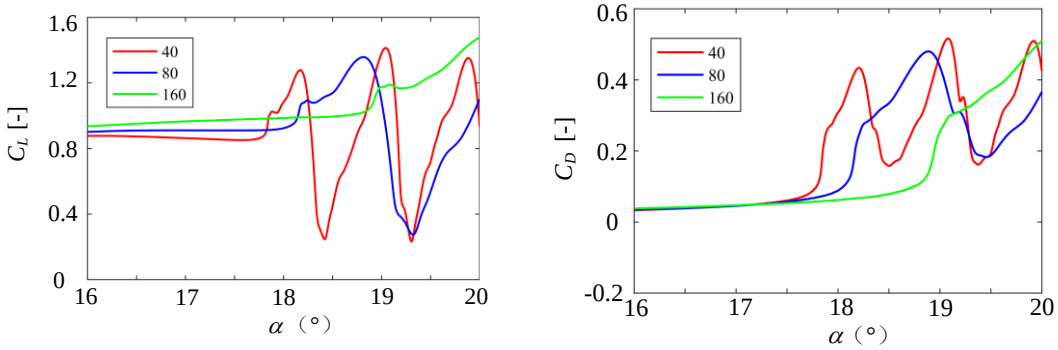

(a) Lift coefficient C_L (b) drag coefficient C_D

Figure 6 Variation of lift coefficient and drag coefficient with α at different angular velocities

Figure 7 shows the streamlines in the leading edge of the hydrofoil at three angular velocities for Reynolds number Re_L =2.0×10^6. When the angle of attack is 17°, the streamlines at the three angular velocities have a good attachment to the wall. When the angle of attack is 18°, the large scale separation vortex is found in the leading edge of the hydrofoil at 40°/s , which indicates the hydrofoil has been in a deep stall stage; at the angular velocity of 80°/s, the trailing edge vortex has been fused with the leading edge separation vortex, which indicates the dynamics hydrofoil is about to enter the deep stall stage; the streamlines in the leading edge still has a good attachment to the wall at the angular velocity of 160°/s. When the angle of attack is 19°, the large-scale separation vortex is found in the leading edge of the hydrofoil region at all the three conditions, which indicates that the dynamics hydrofoil has entered the deep stall stage.

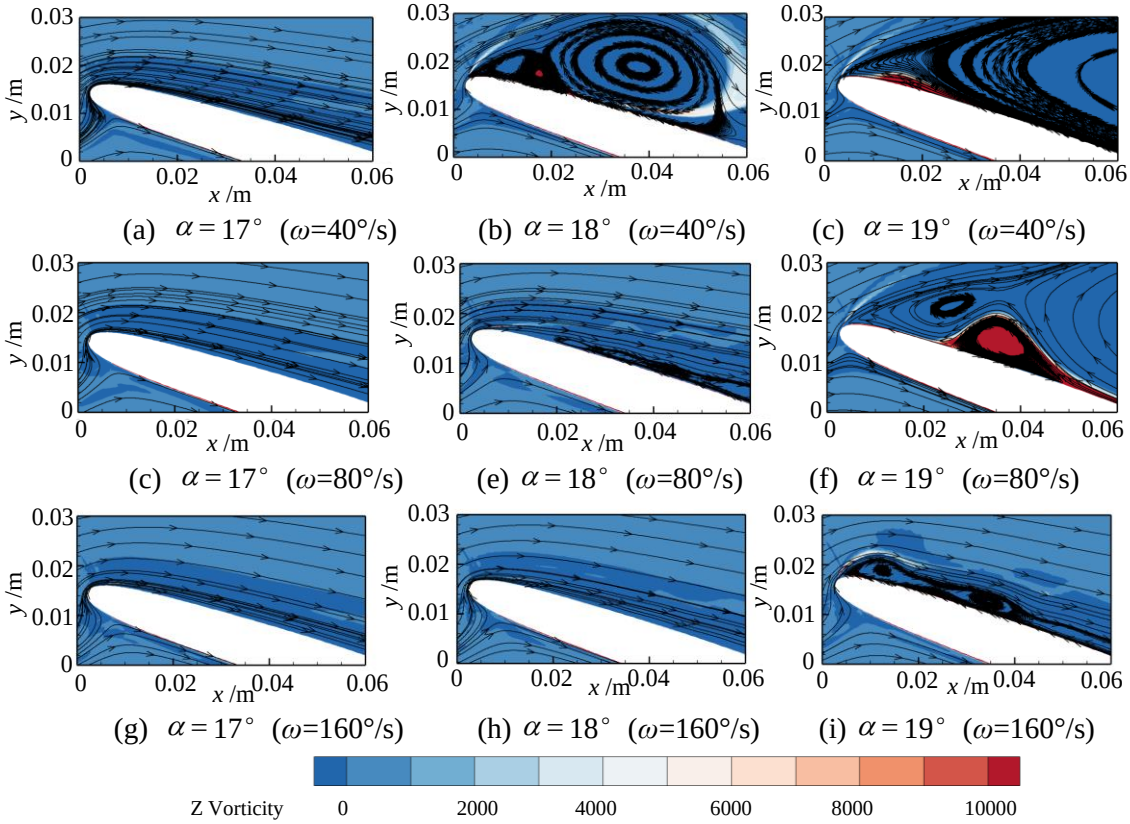

(a) $\alpha = 17°$ (ω=40°/s) (b) $\alpha = 18°$ (ω=40°/s) (c) $\alpha = 19°$ (ω=40°/s)

(c) $\alpha = 17°$ (ω=80°/s) (e) $\alpha = 18°$ (ω=80°/s) (f) $\alpha = 19°$ (ω=80°/s)

(g) $\alpha = 17°$ (ω=160°/s) (h) $\alpha = 18°$ (ω=160°/s) (i) $\alpha = 19°$ (ω=160°/s)

Figure 7 Velocity flow line and vortex near hydrofoil leading edge at different angular velocities

4.3 Effect of Reynolds number on dynamic stall characteristics

In order to investigate the effect of Reynolds number variation on the dynamic stall speed of the hydrofoil, this section calculates and analyses the dynamic hydrofoil at five incoming velocities with an angular velocity ω of 80°/s. The inlet velocities are 6m/s, 12m/s, 16m/s, 20m/s, and 24m/s, and the corresponding chord length Reynolds numbers Re_L are 0.6×10^6, 1.2×10^6, 1.6×10^6, 2.0×10^6 and 2.4×10^6 respectively. Figure 8 gives the variation of lift and drag coefficient with angle of attack at different Reynolds numbers, and it can be seen that changing the Reynolds number, the lift and drag characteristics still show four characteristics stages. In the first two stages, the drag coefficient decreases with increasing Reynolds number, and the lift coefficient increases with increasing Reynolds number. In the fourth stage, the angles of attack of the five Reynolds numbers corresponding to the deep stall are 14.2°, 15.9°, 17.5°, 18.1° and 18.8°, which indicate that the increase of Reynolds number suppresses the generation of hydrofoil deep stall. With the increase of Reynolds number, the oscillation period of hydrofoil stall becomes faster, and the oscillation period under the chord length Reynolds number $Re_L=0.6\times10^6$ is three times that of the corresponding value of $Re_L=2.4\times10^6$.

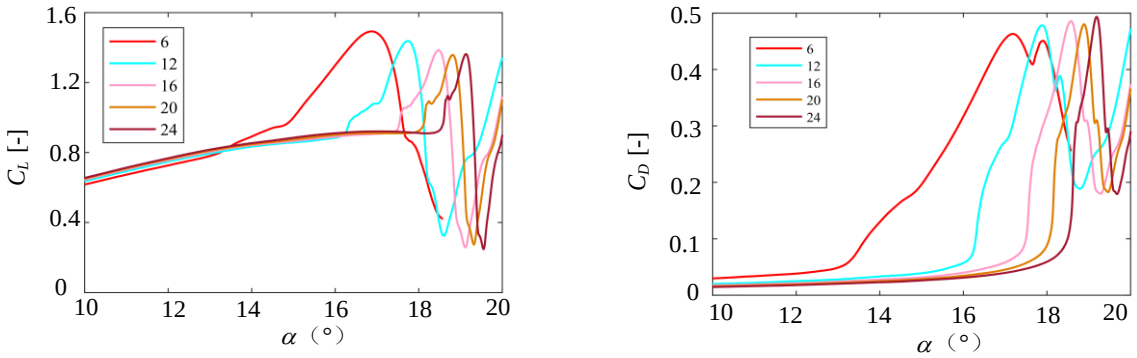

（a）Lift coefficient C_L （b）Drag coefficient C_D

Figure 8 Variation of lift coefficient and drag coefficient with α at different Reynolds numbers

4.4 Dynamic hydrofoil boundary layer properties

To further investigate, the hydrofoil boundary layer characteristics are analysed, Figure 9 shows the dynamic hydrofoil α=0° boundary layer velocity distribution under different conditions.

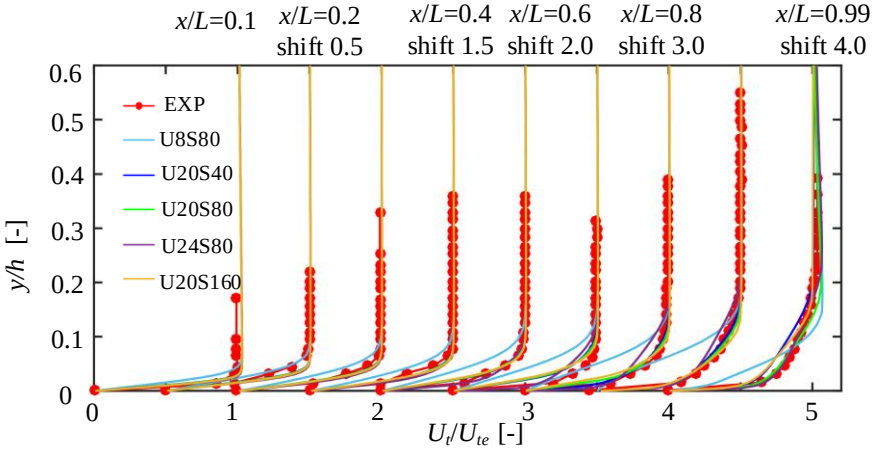

Figure 9 Boundary layer velocity distribution of dynamic hydrofoil at α=0°

In order to facilitate comparison, the boundary layer velocity distribution of the static hydrofoil α=0° with an inlet velocity of 20m/s is added. In the figure, U represents the velocity, and S represents the angular velocity while U8S80 represents the dynamic hydrofoil with an inlet velocity of 8m/s and an angular velocity of 80°/s. From the figure, it can be seen that the variability of the boundary layer velocity distribution under the three angular velocities of the same Reynolds number is small, and the

angular velocity has less effect on the distribution of the boundary layer velocity at the leading and trailing edges of the hydrofoil at α=0°. Under the same angular velocity, the boundary layer velocity distribution at low Reynolds number is more similar to that of the laminar boundary layer, which is the same as the results of the static hydrofoil, the transition is not easily occurred at low Reynolds number. Further comparison of the boundary layer thickness as well as the shape factor distribution is shown in Figure10 and Figure 11. When increasing the angular velocity, the thickness of the boundary layer increases, and the shape factors corresponding to the angular velocities of 40°/s, 80°/s and 160°/s start to fall below 1.5 at 0.8L, 0.7L and 0.6L, respectively, indicating that the transitions are completed at these three positions and the boundary layer is already turbulent, indicating that the larger the angular velocity, the faster the boundary layer transitions. At the same angular velocity, the smaller the Reynolds number, the slower the transition occurs.

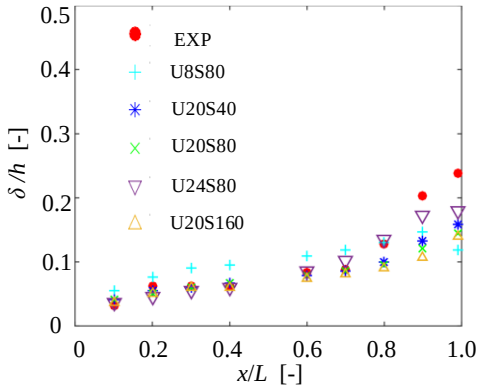

Figure 10 Distribution of relative thickness δ/h of boundary layer at α=0°

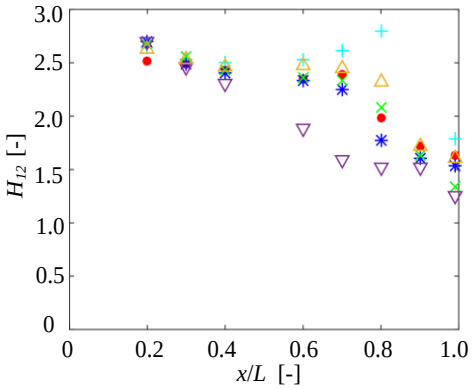

Figure 11 Distribution of boundary layer shape factor for dynamic hydrofoil at α=0°

Figure 12 shows the distribution of the friction coefficients C_f at different conditions when the angle of attack is equal to 0°, 2° and 4°, respectively. Unlike the static hydrofoils, the distribution of friction coefficients on the suction and pressure side of the dynamic hydrofoils at α=0° is not symmetrical, and the suction side transitions earlier than the pressure side. Under the same angular velocity condition, the suction side transitions earlier with the increase of Reynolds number at α=2° and 4°, when the Reynolds number Re_L is 2.4×10^6, the suction side transitions at the leading edge of the hydrofoil, and the pressure side transitions towards the trailing edge of the hydrofoil with the increase of Reynolds number. Under the same Reynolds number condition, the transition position of the hydrofoil suction side at α=0° slowly moves toward the leading edge of the hydrofoil with the increase of angular velocity, and the transition position of hydrofoil pressure surface slowly moves toward the trailing edge of the hydrofoil with the increase of angular velocity. The transition position of hydrofoil suction side slowly moves toward the trailing edge of the hydrofoil with the increase of angular velocity at α=0°, and the transition position of hydrofoil pressure surface remains unchanged with the increase of angular velocity. The transition position of suction side and pressure side remain unchanged as the increase of angular velocity at α=4°.

5. Conclusions

In this paper, the dynamic hydrofoil stall characteristics are investigated by using the SST k-ω turbulence model and the transition model, the conclusions are as follows:

(1) For the study of hydrofoil dynamic stall prediction, it is found that the hydrofoil deep stall calculated by the turbulence model with transition occurred at a much-delayed angle of attack than that calculated by the turbulence model without transition, and the difference between the two models are small before the stall inception.

(2) Hydrofoil dynamic stall can be divided into four stages: initial stage, development stage, stall inception stage and deep stall stage. In the initial stage and the development stage, the lift and drag characteristics are influenced by the shedding vortex. In the stall inception stage and the deep stall stage, the lift and drag characteristics are affected by the leading edge vortex and the trailing edge vortex.

(3) The occurrence of dynamic hydrofoil deep stall will delay as the angular velocity and Reynolds number increase because of accelerating the boundary layer transition. The distribution of friction coefficients on the suction and pressure sides of the dynamic hydrofoils is not symmetrical, and the suction side transitions earlier than the pressure side.

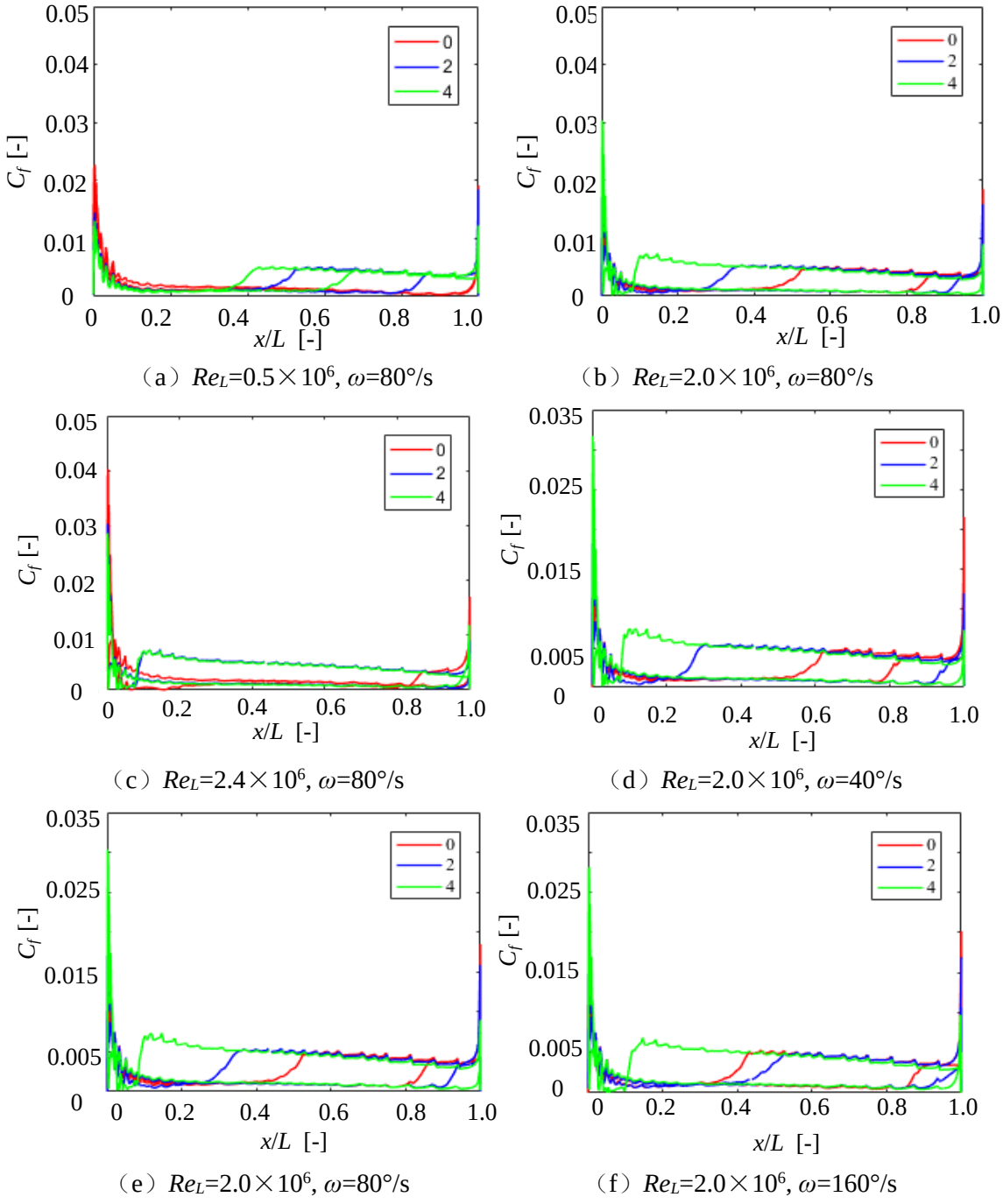

（a）Re_L=0.5×10^6, ω=80°/s

（b）Re_L=2.0×10^6, ω=80°/s

（c）Re_L=2.4×10^6, ω=80°/s

（d）Re_L=2.0×10^6, ω=40°/s

（e）Re_L=2.0×10^6, ω=80°/s

（f）Re_L=2.0×10^6, ω=160°/s

Figure 12 Distribution of wall friction coefficient at different angular velocities and Reynolds number

Acknowledgments

This work was supported by the National Science Foundation of China (NSFC, Grant Nos. 51836010, 51779258, and 51839001), The authors also appreciated the High-Performance Computing of Eindhoven University of Technology.

References

[1] Cervantes M, Trivedi C H, Dahlhaug O G. Francis-99 Workshop 1: steady operation of Francis turbines[C]//*Journal of Physics: Conference Series. IOP Publishing*, 2015, **579(1)**: 011001.
[2] Tang Y, Wang F, Wang C, Hong Y, Yao Z, Tang X. Low-frequency oscillation characteristics of flow for NACA66 hydrofoil under critical stall condition[J]. *Renewable Energy*, 2021, **172**: 983-997.
[3] Ye C, Wang C, Zi D, Tang Y, van Esch B, Wang F. Improvement of the SST γ-$Re_{\theta t}$ transition model for flows along a curved hydrofoil[J]. *Journal of Hydrodynamics*, 2021, **33(3)**: 520-533.
[4] Karbasian H, Kim K. Numerical investigations on flow structure and behavior of vortices in the dynamic stall of an oscillating pitching hydrofoil[J]. *Ocean Engineering*, 2016, **127**: 200-211.
[5] Zhang M, Liu T, Huang B, Wu Q, Wang G. Hydrodynamic characteristics and flow structures of pitching hydrofoil with special emphasis on the added force effect[J]. *Renewable Energy*, 2020, **157**: 560-573.
[6] Almohammadi K, Ingham D, Ma L, Pourkashanian M. Modeling dynamic stall of a straight blade vertical axis wind turbine[J]. *Journal of Fluids & Structures*, 2015, **57**: 144-158.
[7] Seyednia M, Masdari M, Vakilipour S. Numerical assessment of a deformable trailing-edge flap on aerodynamic load control of a pitching S809 airfoil using OpenFOAM[J]. *Proceedings of the Institution of Mechanical Engineers, Part A: Journal of Power and Energy*, 2019, **233(7)**: 890-900.
[8] Rijpkema D, Baltazar J, Falcao de Campos J. Viscous flow simulations of propellers in different Reynolds number regimes[C]//*Proceedings of the 4th International Symposium on Marine Propulsors*, Austin, USA, 2015.
[9] Li H, Huang Q, Pan G, Dong X. Assessment of transition modeling for the unsteady performance of a pump-jet propulsor in model scale[J]. *Applied Ocean Research*, 2021, **108(7)**: 102537.
[10] Bhattacharyya A, Krasilnikov V, Steen S. Scale effects on open water characteristics of a controllable pitch propeller working within different duct designs[J]. *Ocean Engineering*, 2016, **112(15)**: 226-242.
[11] Bhattacharyya A, Neitzel J, Steen S. Influence of flow transition on open and ducted propeller characteristics[C]// *Proceedings of the 4th International Symposium on Marine Propulsors*, Austin, USA. 2015.
[12] Langtry R, Menter F. Correlation-based transition modeling for unstructured parallelized computational fluid dynamics codes[J]. AIAA journal, 2009, **47(12)**: 2894-2906.
[13] Münch C, Ausoni P, Braun O, Farhat M, Avellan F. Fluid–structure coupling for an oscillating hydrofoil[J]. *Journal of Fluids and Structures*, 2010, **26(6)**: 1018-1033.
[14] Delafin P L, Deniset F, Astolfi J A. Effect of the laminar separation bubble induced transition on the hydrodynamic performance of a hydrofoil[J]. *European Journal of Mechanics-B/Fluids*, 2014, **46**: 190-200.